Check for updates

JAMES | Journal of Advances in Modeling Earth Systems®

RESEARCH ARTICLE
10.1029/2024MS004319

Detecting Instantaneous Tidal Signals in Ocean Models Utilizing Streaming Band-Pass Filters

Chengzhu Xu[1] and **Edward D. Zaron**[1]

[1]College of Earth, Ocean, and Atmospheric Sciences, Oregon State University, Corvallis, OR, USA

Key Points:

- The streaming band-pass filter can detect sinusoidal motions at tidal frequencies from the instantaneous model output
- The filtering algorithm is computationally efficient and is capable of capturing the temporal variation of tidal signals
- The filters can be utilized to parameterize frequency-dependent internal wave drag and to de-tide model output

Correspondence to:
C. Xu,
chengzhu.xu@oregonstate.edu

Citation:
Xu, C., & Zaron, E. D. (2024). Detecting instantaneous tidal signals in ocean models utilizing streaming band-pass filters. *Journal of Advances in Modeling Earth Systems*, *16*, e2024MS004319. https://doi.org/10.1029/2024MS004319

Received 1 MAR 2024
Accepted 14 SEP 2024

Abstract Through the implementation of a streaming filter, output of numerical ocean simulations can be band-pass filtered at tidal frequencies while the model is running, yielding time series of sinusoidal motions consisting of tidal signals in the filter's target frequency band. The filtering algorithm is developed from a system of two ordinary differential equations that represents the motion of a damped harmonic oscillator. The filter's response to a broadband input signal is unity at its target frequency but vanishes toward the low and high frequency limits. The decay of the filter response is controlled by a dimensionless parameter, which determines the filter's bandwidth. As a result, the filter allows signals within a small frequency band around its target frequency to pass through, while blocking signals outside of its target frequency band. In this work, the filtering algorithm is implemented into the barotropic solver of the Modular Ocean Model version 6 (MOM6) for determining the instantaneous tidal velocities of the semi-diurnal and diurnal tides. Utilizing the filters, the frequency-dependent internal wave drag is applied to the semi-diurnal and diurnal frequency bands separately. The simulation results suggest that the performance of the algorithm is consistent with the filter transfer function in Fourier space. Potential applications of the algorithm also include de-tiding the model output for nested regional ocean models, especially those for the purpose of operational forecasting.

Plain Language Summary In this work, we developed a computationally efficient algorithm for detecting tidal signals from the instantaneous model output, without needing to harmonically analyze the entire time series of model output. This is achieved through the construction of a streaming filter, which takes the instantaneous model output as the input and returns a time series consisting of tidal motions at its target frequency band as the output, in a process that effectively allows signals within its target frequency band to pass through and blocks signals outside of its target frequency band. Unlike the conventional harmonic analysis, the band-pass filtering process does not require information from any of the previous or future time steps. The filtering algorithm is implemented and validated in a global ocean model. The filters can be utilized to parameterize frequency-dependent internal wave drag, as demonstrated in this work, and to remove tidal signals from the model output, which has potential application in regional ocean forecasting systems.

1. Introduction

In the global oceans, tidal signals (amplitudes and phases) are usually determined by means of harmonic analysis, provided that data of reasonable temporal resolution and record length are available (Foreman et al., 2009). There are some limitations, however. First, in order to perform harmonic analysis, the entire time series must be available a priori. Second, performing harmonic analysis over a large geographical extent tends to be a computationally expensive task for two-dimensional data sets and impractical for three-dimensional data sets. Moreover, tidal amplitudes and phases determined through the harmonic analysis are constant in time, unless the harmonic analysis is repeated in a sliding time window, which further increases the computational cost. Because of these limitations, it is generally difficult and often impractical to use the conventional harmonic analysis for determining the instantaneous tidal signals in numerical simulations performed in the time domain.

Nevertheless, there are instances in which knowing the instantaneous tidal signals while the model is running is desired. One such instance is the parameterization of frequency-dependent internal wave drag in global ocean models. Input of tidal energy into the world's oceans is about 3.5 TW (Egbert & Ray, 2003), of which about 30% is dissipated in the deep ocean due to barotropic-to-baroclinic energy conversion (Egbert & Ray, 2000, 2001). The conversion acts as a linear drag on the barotropic flow and is often referred to as the "internal wave drag" or the "wave drag" (Arbic, 2022). In barotropic models, the entire barotropic-to-baroclinic conversion is parameterized. Even in baroclinic models which may partially resolve low-mode energy conversion, parameterization is still

© 2024 The Author(s). Journal of Advances in Modeling Earth Systems published by Wiley Periodicals LLC on behalf of American Geophysical Union. This is an open access article under the terms of the Creative Commons Attribution-NonCommercial-NoDerivs License, which permits use and distribution in any medium, provided the original work is properly cited, the use is non-commercial and no modifications or adaptations are made.

19422466, 2024, 10, Downloaded from https://agupubs.onlinelibrary.wiley.com/doi/10.1029/2024MS004319, Wiley Online Library on [12/06/2025]. See the Terms and Conditions (https://onlinelibrary.wiley.com/terms-and-conditions) on Wiley Online Library for rules of use; OA articles are governed by the applicable Creative Commons License

needed in order to represent conversion due to unresolved higher mode waves and energy loss due to wave breaking (Buijsman et al., 2016). Most of the internal wave parameterization schemes are based on either the linear theory (e.g., Garner, 2005; Nycander, 2005) or dimensional analysis (e.g., Jayne & St. Laurent, 2001; Zaron & Egbert, 2006). Both types of parameterization schemes suggest that the wave drag is frequency dependent, with a scaling factor given by $\sqrt{1-f^2/\omega^2}$, where f is the Coriolis frequency and ω is the tidal frequency. This implies that the energy dissipation due to semi-diurnal tides is different from that due to diurnal tides. Moreover, applying the drag to the broadband barotropic velocity field would disproportionally affect the low-frequency motions, which has significantly implications on climate simulations. However, due to difficulties in determining the instantaneous tidal velocities in numerical simulations performed in the time domain, the frequency-dependent scaling factor is often neglected.

Another task that would benefit from knowing the instantaneous tidal signals and their temporal variation is de-tiding the model output in nested ocean models. Because tides in global and basin-scale models tend to be less accurate than tides in satellite altimeter-constrained data assimilative tide models (e.g., TPXO9 by Egbert and Erofeeva (2002)), tidal signals are often removed from their output when they are used to force smaller-scale, higher-resolution regional models. This allows tides in the regional models to be forced by data assimilative models (e.g., Paquin et al., 2020). De-tiding by means of harmonic analysis can be computationally expensive, and impractical for two-way nested models, since the parent and child models must be running at the same time. Moreover, the conventional harmonic analysis may not fully and accurately capture the temporal variation of tidal signals, especially at locations where tides exhibit strong seasonal variability (e.g., where there exists seasonal ice coverage; Rotermund et al., 2021). Knowing the instantaneous tidal elevations and velocities would allow for efficient de-tiding without needing to harmonically analyze the model output data. This could be particularly helpful for improving the performance of regional ocean forecasting systems, since the model output must be available in a timely manner.

In both instances discussed above, the goal is to determine the sinusoidal motions at tidal frequencies while the model is running. In fact, it is possible to achieve this goal without performing harmonic analysis, because the time series representing the sinusoidal motions does not have to be constructed from the tidal amplitudes and phases. In this work, we will show that such a time series can be obtained by band-pass filtering the model output at tidal frequencies through the implementation of a streaming filter. In Section 2 of this paper, we will derive the filter equations and discuss the filter's response to a broadband input signal. In Section 3, some guidance on choosing the filter's bandwidth will be provided. In Section 4, the algorithm is implemented and validated in a global barotropic ocean model, developed based on Modular Ocean Model version 6 (MOM6), and the application to the parameterization of frequency-dependent internal wave drag is demonstrated. Finally, in Section 5, a brief summary of this work will be provided.

2. Methods

2.1. Filter Design

Let $u(t)$ denote a time series that is broadband in the frequency domain, consisting of tidal signals at various frequencies as well as the noise. To detect the tidal signal at frequency ω_1, consider the system of equations for a damped harmonic oscillator,

$$\frac{du_1}{dt} = -\omega_1 [s_1(t) + \alpha u_1(t) - g(t)], \quad \alpha \geq 0, \tag{1a}$$

$$\frac{ds_1}{dt} = \omega_1 [u_1(t) - \beta s_1(t) - f(t)], \quad \beta \geq 0. \tag{1b}$$

In this system, ω_1 is the resonant frequency, f and g represent inputs into the system, and α and β are the damping coefficients. It is important to note that, in order for the system to be stable for arbitrary bounded inputs, α and β cannot be both zeros. Assuming the inputs are linear functions of u, that is,

$$f(t) = f_1 u(t), \quad \text{and} \quad g(t) = g_1 u(t), \tag{2}$$

19422466, 2024, 10, Downloaded from https://agupubs.onlinelibrary.wiley.com/doi/10.1029/2024MS004319, Wiley Online Library on [12/06/2025]. See the Terms and Conditions (https://onlinelibrary.wiley.com/terms-and-conditions) on Wiley Online Library for rules of use; OA articles are governed by the applicable Creative Commons License

where f_1 and g_1 are real coefficients, it is possible to configure this system as a band-pass filter, so that u_1 consists primarily of the tidal signal at frequency ω_1 (and s_1 is a dummy variable). Represented in the frequency domain, this system may be written as

$$i\omega^*\tilde{u}_1 = -\omega_1(\tilde{s}_1 + \alpha\tilde{u}_1 - g_1\tilde{u}), \tag{3a}$$

$$i\omega^*\tilde{s}_1 = \omega_1(\tilde{u}_1 - \beta\tilde{s}_1 - f_1\tilde{u}), \tag{3b}$$

where ω^* is the broadband input (forcing) frequency, and the tilde denotes the Fourier transforms of the original variables. To simplify the analysis and notation, we shall non-dimensionalize the input frequency by the target frequency and define $\omega = \omega^*/\omega_1$. With some algebra, a relationship between $\tilde{u}_1$ and $\tilde{u}$ can be established,

$$\tilde{u}_1 = \left[\frac{f_1 + (\beta + i\omega)g_1}{(\alpha + i\omega)(\beta + i\omega) + 1}\right]\tilde{u}. \tag{4}$$

To determine f_1 and g_1, we impose a constraint that if $\omega = 1$, then $\tilde{u} = \tilde{u}_1$, such that at the target frequency, u_1 captures the full signal from the inputs. This implies that

$$\frac{f_1 + (\beta + i)g_1}{(\alpha + i)(\beta + i) + 1} = 1.$$

From the real and imaginary parts of this equation, two equations for the real coefficients can be obtained, from which f_1 and g_1 can be solved,

$$f_1 = -\beta^2, \quad \text{and} \quad g_1 = \alpha + \beta. \tag{5}$$

This implies that the relation between $\tilde{u}_1$ and $\tilde{u}$ is given by

$$\tilde{u}_1 = \left[\frac{\alpha\beta + i(\alpha + \beta)\omega}{(\alpha\beta - \omega^2 + 1) + i(\alpha + \beta)\omega}\right]\tilde{u}, \tag{6}$$

and that the filter equations are given by

$$\frac{du_1}{dt} = -\omega_1\left[s_1(t) + \alpha u_1(t) - (\alpha + \beta)u(t)\right], \tag{7a}$$

$$\frac{ds_1}{dt} = \omega_1\left[u_1(t) - \beta s_1(t) + \beta^2 u(t)\right]. \tag{7b}$$

In the context of a streaming band-pass filter, ω_1 represents the target frequency of the filter, while α and β determine the bandwidth of the filter.

2.2. Filter Response

The filter's response to a broadband input is determined by the complex coefficient in Equation 6. Here and henceforth, we shall refer to it as the "filter transfer function" and denote it by $\mathcal{A}(\omega;\alpha,\beta)$,

$$\mathcal{A}(\omega;\alpha,\beta) = \frac{\alpha\beta + i(\alpha + \beta)\omega}{(\alpha\beta - \omega^2 + 1) + i(\alpha + \beta)\omega}, \quad \omega \geq 0, \quad \alpha \geq 0, \quad \beta \geq 0. \tag{8}$$

Here, we emphasize again that α and β cannot be both zeros. The real and imaginary parts of $\mathcal{A}$ are given by

$$\Re(\mathcal{A}) = \frac{\alpha\beta(\alpha\beta - \omega^2 + 1) + (\alpha + \beta)^2\omega^2}{(\alpha\beta - \omega^2 + 1)^2 + (\alpha + \beta)^2\omega^2}, \tag{9a}$$

19422466, 2024, 10, Downloaded from https://agupubs.onlinelibrary.wiley.com/doi/10.1029/2024MS004319, Wiley Online Library on [12/06/2025]. See the Terms and Conditions (https://onlinelibrary.wiley.com/terms-and-conditions) on Wiley Online Library for rules of use; OA articles are governed by the applicable Creative Commons License

and

$$\Im(\mathcal{A}) = \frac{\omega(\alpha+\beta)\left(1-\omega^2\right)}{(\alpha\beta-\omega^2+1)^2+(\alpha+\beta)^2\omega^2}, \tag{9b}$$

respectively, while the magnitude and argument of $\mathcal{A}$ are given by

$$|\mathcal{A}| = \sqrt{[\Re(\mathcal{A})]^2+[\Im(\mathcal{A})]^2}, \quad \text{and} \quad \arg(\mathcal{A}) = \tan^{-1}\left[\frac{\Im(\mathcal{A})}{\Re(\mathcal{A})}\right], \tag{10}$$

respectively. For an output signal, $|\mathcal{A}|$ characterizes the amplitude change due to filtering, while $\arg(\mathcal{A})$ characterizes the phase shift due to filtering. It can be shown that the filter transfer function has the following properties for all $\alpha \geq 0$ and $\beta \geq 0$:

1. $\Re(\mathcal{A}) = 1$ and $|\mathcal{A}| = 1$ at $\omega = 1$,
2. $\Re(\mathcal{A}) \geq 0$ and $|\mathcal{A}| \geq 0$ for all $\omega \geq 0$,
3. $\Im(\mathcal{A}) = 0$ and $\arg(\mathcal{A}) = 0$ at $\omega = 1$,
4. $\Im(\mathcal{A}) \geq 0$ and $\arg(\mathcal{A}) \geq 0$ if $\omega < 1$, while $\Im(\mathcal{A}) \leq 0$ and $\arg(\mathcal{A}) \leq 0$ if $\omega > 1$.

Additionally, the filter transfer function has the following properties:

Theorem 1: In the log-linear scale of ω, $\Re(\mathcal{A})$ and $|\mathcal{A}|$ are reflectional symmetric about $\omega = 1$ if and only if either $\alpha = 0$ or $\beta = 0$, whereas $\Im(\mathcal{A})$ and $\arg(\mathcal{A})$ are rotational symmetric about $\omega = 1$ if and only if either $\alpha = 0$ or $\beta = 0$.
Theorem 2: $|\mathcal{A}| \leq 1$ for all $\omega \geq 0$ if and only if either $\alpha = 0$ or $\beta = 0$. Otherwise, there exists a small frequency band to the right of $\omega = 1$ in which $|\mathcal{A}| > 1$.
Theorem 3: If either $\alpha = 0$ or $\beta = 0$, then $\Re(\mathcal{A})$, $\Im(\mathcal{A})$ and $|\mathcal{A}|$ all vanish in both low and high frequency limits, while $\lim_{\omega\to 0} \arg(\mathcal{A}) = \frac{\pi}{2}$ and $\lim_{\omega\to\infty} \arg(\mathcal{A}) = -\frac{\pi}{2}$. If α and β are both non-zero, then $\Re(\mathcal{A})$ and $|\mathcal{A}|$ do not vanish completely in the low frequency limit, while $\arg(\mathcal{A}) \to 0$ in the low frequency limit.

Proofs of the above theorems are provided in Appendix A. According to these theorems, it is necessary to set either α or β to be zero, in order for the filter to be centered at the target frequency and to minimize the signal picked up from the low frequency limit. Without loss of generality, we shall set $\beta = 0$ and reformulate the filter equations for the remainder of this paper,

$$\frac{du_1}{dt} = -\omega_1[s_1(t) + \alpha u_1(t) - \alpha u(t)], \quad \alpha > 0, \tag{11a}$$

$$\frac{ds_1}{dt} = \omega_1 u_1(t). \tag{11b}$$

The filter transfer function of the above system is given by

$$\mathcal{A}(\omega;\alpha) = \frac{i\alpha\omega}{(1-\omega^2)+i\alpha\omega}, \quad \omega \geq 0, \quad \alpha > 0, \tag{12}$$

whose real and imaginary parts are given by

$$\Re(\mathcal{A}) = \frac{\alpha^2\omega^2}{(1-\omega^2)^2+\alpha^2\omega^2}, \quad \text{and} \quad \Im(\mathcal{A}) = \frac{\alpha\omega\left(1-\omega^2\right)}{(1-\omega^2)^2+\alpha^2\omega^2}, \tag{13}$$

respectively. This filter transfer function can be visualized in Figure 1.

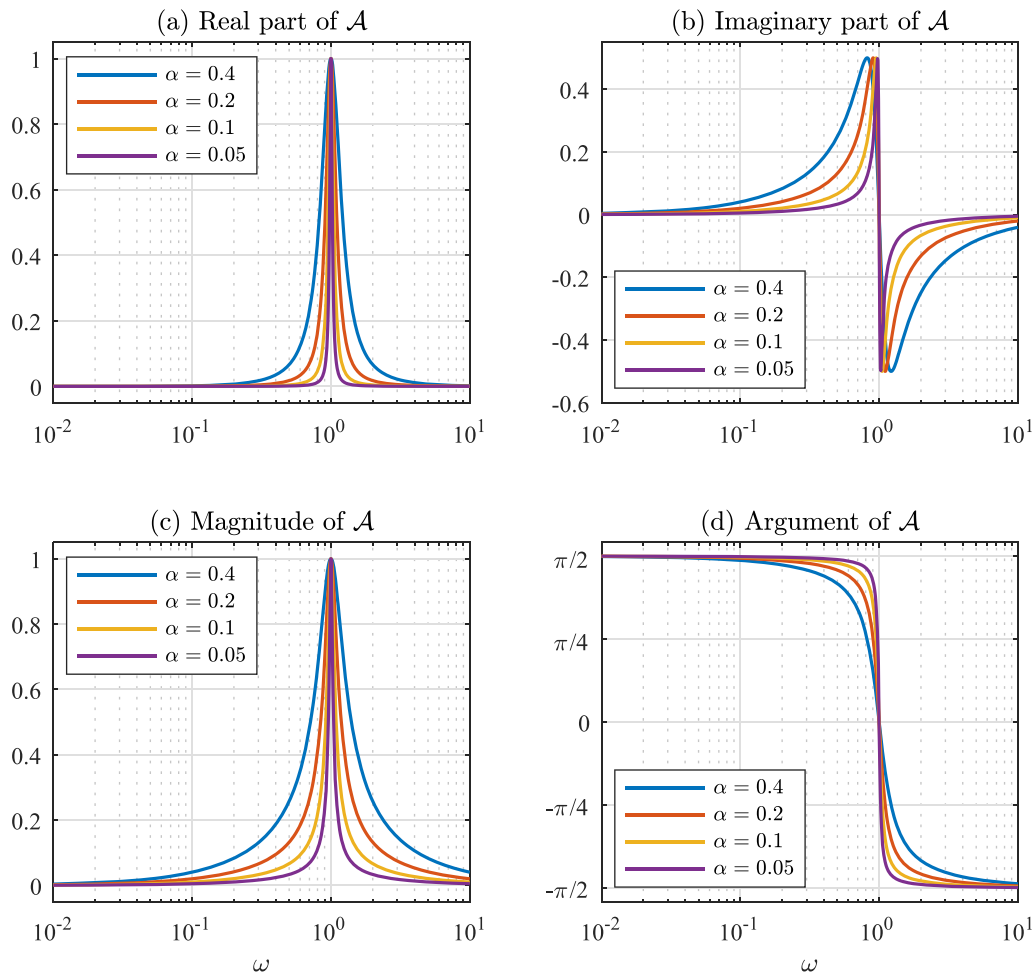

Figure 1. Visualization of the filter transfer function defined by Equation 12.

2.3. Diagnostic Tool

For an input signal of frequency other than the filter's target frequency, the effects of filtering are an amplitude reduction, determined by $|\mathcal{A}|$, and a phase shift, determined by $\arg(\mathcal{A})$. This implies that the strength of the filtering effects, or the difference between the input and output signals, depends on ω, the proximity of the input and target frequencies, and α, the filter's bandwidth. The combined effects of amplitude reduction and phase shift can be measured by the root mean squared error (RMSE), defined by

$$\text{RMSE} = \sqrt{\langle [u(t) - u_1(t)]^2 \rangle}, \tag{14}$$

where the angle brackets indicate time average. Because the output frequency is determined by the input frequency (instead of the filter's target frequency), it is possible to express the RMSE in terms of the amplitude C and the phase θ,

$$\text{RMSE} = \sqrt{0.5\left(C_u^2 + C_{u_1}^2\right) - C_u C_{u_1} \cos\left(\theta_u - \theta_{u_1}\right)} = C_u \sqrt{0.5\left(1 + |\mathcal{A}|^2\right) - \Re(\mathcal{A})}. \tag{15}$$

When normalized by $\sqrt{0.5} C_u$, the RMSE quantifies the signal blocked by the filter,

$$B(\omega; \alpha) = \sqrt{1 + |\mathcal{A}|^2 - 2\Re(\mathcal{A})}. \tag{16}$$

19422466, 2024, 10, Downloaded from https://agupubs.onlinelibrary.wiley.com/doi/10.1029/2024MS004319, Wiley Online Library on [12/06/2025]. See the Terms and Conditions (https://onlinelibrary.wiley.com/terms-and-conditions) on Wiley Online Library for rules of use; OA articles are governed by the applicable Creative Commons License

19422466, 2024, 10, Downloaded from https://agupubs.onlinelibrary.wiley.com/doi/10.1029/2024MS004319, Wiley Online Library on [12/06/2025]. See the Terms and Conditions (https://onlinelibrary.wiley.com/terms-and-conditions) on Wiley Online Library for rules of use; OA articles are governed by the applicable Creative Commons License

3. Discussion

3.1. Optimal Choice of α

For clarity of presentation, we shall refer to a filter by its target frequency. As an example, consider the M_2 filter whose target frequency is $\omega_1 = 1.4 \times 10^{-4}$ s^{-1}. For four different values of α between 0.05 and 0.4, the effects of filtering are shown in Figure 2. In the diurnal frequency band, the filtering leads to an amplitude reduction of more

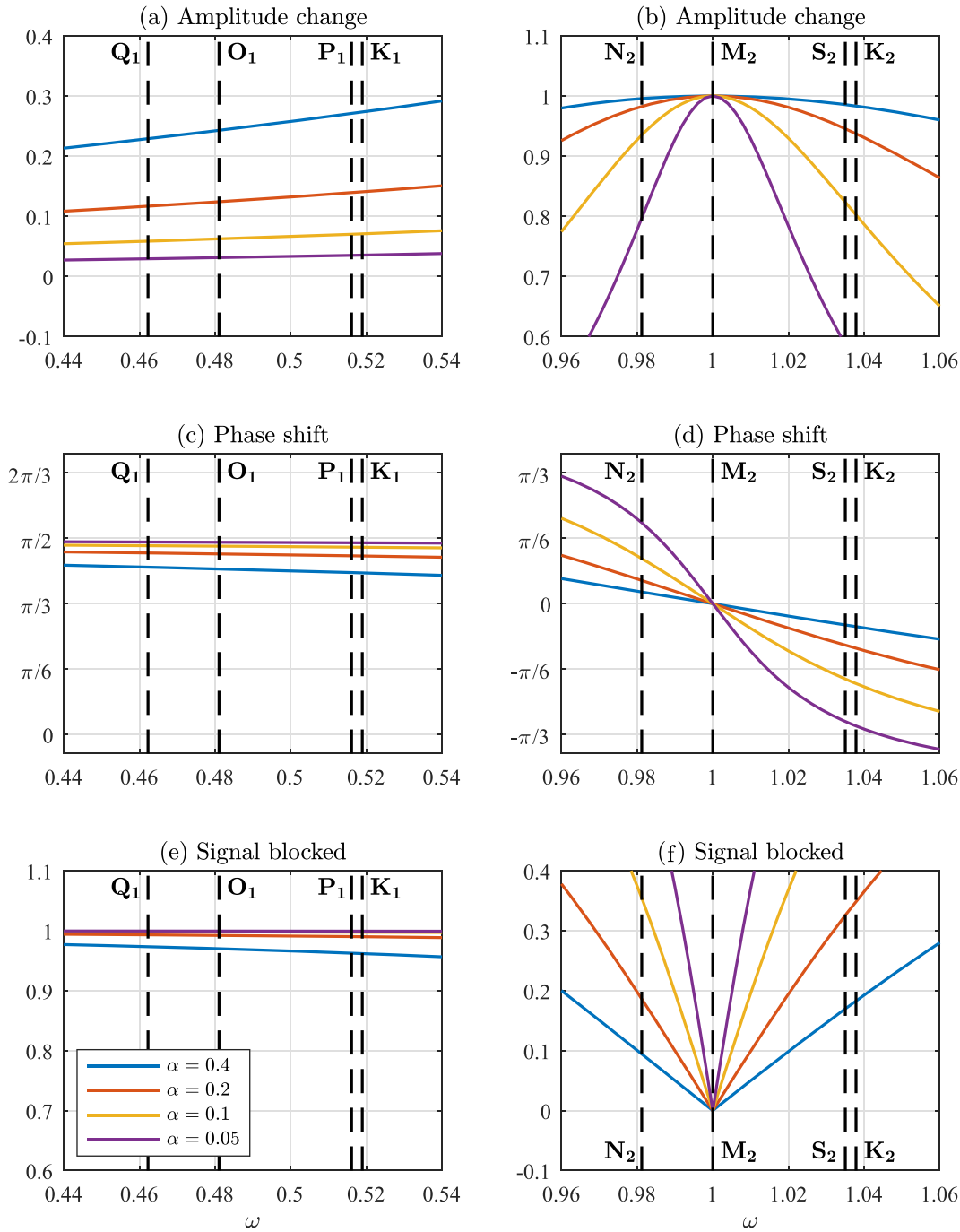

Figure 2. Effects of filtering of the M_2 filter on the diurnal and semi-diurnal frequency bands. Here, the amplitude change is quantified by $|\mathcal{A}|$, the phase shift is quantified by $\arg(\mathcal{A})$, and the proportion of signal blocked by the filter is quantified by B defined by Equation 16.

19422466, 2024, 10, Downloaded from https://agupubs.onlinelibrary.wiley.com/doi/10.1029/2024MS004319, Wiley Online Library on [12/06/2025]. See the Terms and Conditions (https://onlinelibrary.wiley.com/terms-and-conditions) on Wiley Online Library for rules of use; OA articles are governed by the applicable Creative Commons License

Table 1
Effects of Filtering of the M_2 *Filter Measured by* $|\mathcal{A}|$*, the Amplitude Change,* $\arg(\mathcal{A})$*, the Phase Shift, and B, the Proportion of Signal Blocked by the Filter, for Different Values of* α*, With the Input Frequencies Being the* S_2 *and* K_1 *Frequencies*

	Input at S_2 frequency			Input at K_1 frequency		
α	$\lvert\mathcal{A}\rvert$	$\arg(\mathcal{A})$	B	$\lvert\mathcal{A}\rvert$	$\arg(\mathcal{A})$	B
1	0.9976	−3.94°	6.88%	0.5790	54.62°	81.53%
0.7	0.9952	−5.62°	9.80%	0.4452	63.57°	89.54%
0.4	0.9855	−9.78°	16.98%	0.2733	74.14°	96.19%
0.2	0.9454	−19.01°	32.58%	0.1406	81.92°	99.01%
0.1	0.8234	−34.57°	56.74%	0.0708	85.94°	99.75%
0.05	0.5873	−54.04°	80.94%	0.0355	87.97°	99.94%
0.02	0.2787	−73.82°	96.04%	0.0142	89.19°	99.99%
0.01	0.1436	−81.74°	98.96%	0.0071	89.59°	100.00%

than 70% and a phase shift of almost 90°. As a result, more than 95% of the diurnal signal is blocked by the filter. In the semi-diurnal frequency band, however, with a sufficiently large bandwidth, a significant amount of signal can pass through the filter. For example, with $\alpha = 0.4$, the amplitude reduction of the S_2 signal is less than 1.5%, while the phase shift of the S_2 signal is less than 10°. As a result, less than 17% of the S_2 signal is blocked by the M_2 filter. Some quantitative measurements of the effects of the M_2 filter can be found in Table 1, while the proportion of various input signal that can pass through the M_2 and K_1 filters (the latter has the target frequency $\omega_1 = 7.3 \times 10^{-5}$ s^{-1}) as a function of α can be visualized in Figure 3.

The above analysis provides some insights into how the filters should be constructed in practice. Most importantly, there does not exist a universally applicable criterion for the optimal choice of α. Instead, the optimal choice depends on the application. For example, suppose that at a certain location there exist very strong semi-diurnal tides but weak diurnal tides. In this case, a single semi-diurnal filter with a moderate bandwidth will allow the majority of semi-diurnal tidal signals to pass through, while filtering out other high and low frequency motions. For example, Table 1 shows that with $\alpha = 0.7$, about 90% of the S_2 signal can pass through the M_2 filter, with a phase shift of about 6°, whereas only 10% of the K_1 signal can pass through the M_2 filter. Note that the phase shift of the S_2 signal will translate into the phase shift of the spring-neap cycle in the output signal, and whether or not this is acceptable depends on the application. To block more signal from the diurnal frequency band without decreasing the filter's bandwidth, the filter's target frequency can be shifted toward the S_2 frequency, so that it is located further away from the diurnal frequency band. If, for some reason, it is necessary to block the S_2 signal (e.g., to remove the phase shift in the spring-neap cycle by constructing an S_2 filter), then Table 1 suggests that α of the M_2 filter should be 0.02 or less, so that less than 4% of the input S_2 signal will pass through the M_2 filter.

In contrast, Figure 3b shows that the K_1 filter is not very effective in band-passing the Q_1 or O_1 signal while blocking the semi-diurnal signals at the same time. This is because the Q_1 and O_1 frequencies are located relatively farther away from the K_1 frequency and are on the opposite side of the frequency spectrum from the semi-diurnal frequency band. In this case, depending on the relative importance of the Q_1 and O_1 tides, it might be necessary to reduce the bandwidth of the K_1 filter and to construct another filter with relatively small α, in order to band-pass the Q_1 and O_1 signals.

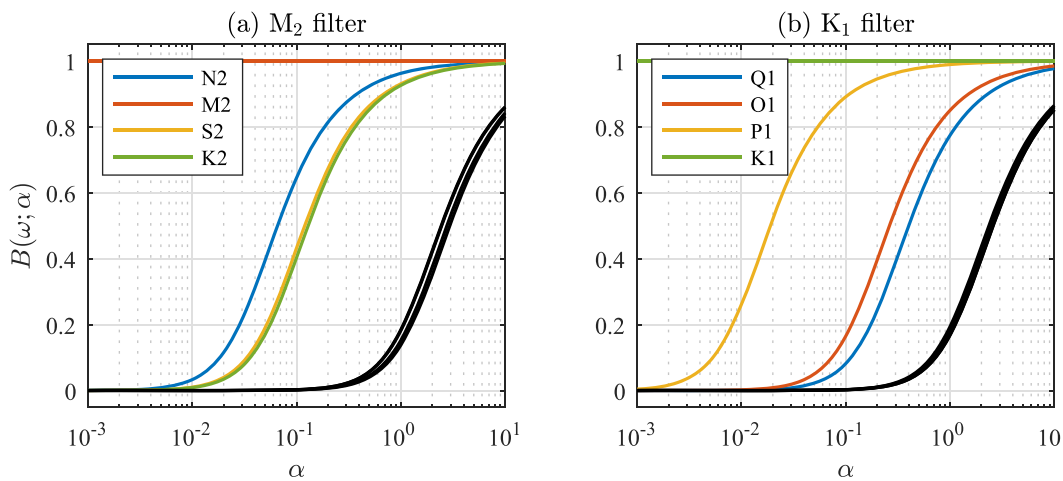

Figure 3. Proportion of input signal that passes through the M_2 and K_1 filters, measured by $(1 - B)$ as a function of α defined by Equation 16. The input frequencies are those of the eight major tidal constituents, Q_1, O_1, P_1, K_1, N_2, M_2, S_2, and K_2. In Panel (a), curves with input frequencies in the diurnal frequency band are shown in black, whereas in panel (b), curves with input frequencies in the semi-diurnal frequency band are shown in black.

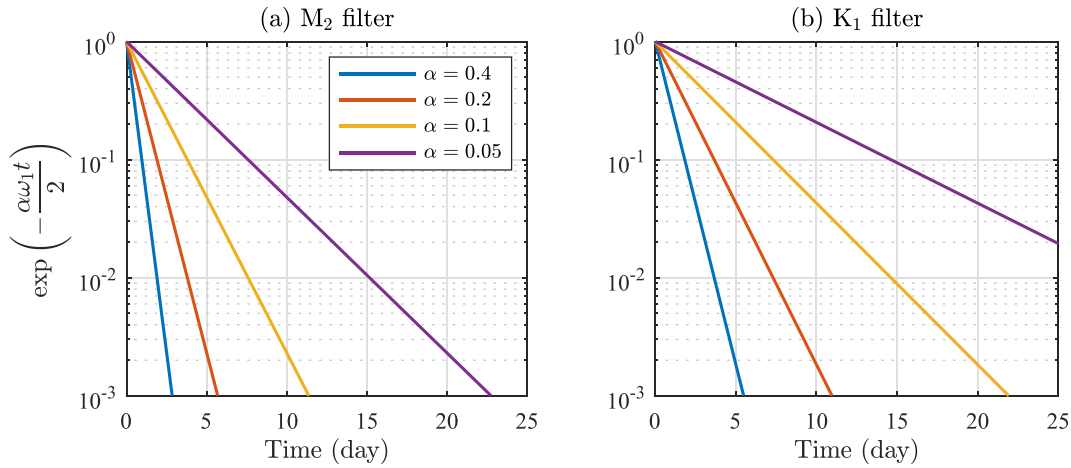

Figure 4. Normalized amplitude of the transient solutions, $\exp(-\alpha\omega_1 t/2)$, for (a) the M_2 filter and (b) the K_1 filter with different values of α between 0.05 and 0.4.

3.2. Transient Solutions to the Filter Equations

So far, the analyses have been based on Fourier transforms of the filter equations in an unbounded time domain, and the filter responses discussed are only applicable to the equilibrium solutions of the filter equations. Nevertheless, there also exist transient solutions that represent the decay of the initial conditions. The homogeneous version of the system of equation (Equation 11) can be represented in the form

$$\frac{d^2u_1}{dt^2} + \alpha\omega_1\frac{du_1}{dt} + \omega_1^2 u_1 = 0, \tag{17}$$

which is a typical second-order constant-coefficient scalar linear homogeneous ordinary differential equation. Solving this equation (e.g., Chapter 4 of Trefethen et al. (2018)) yields solutions of the form

$$u_1(t) = \exp\left[\frac{\omega_1}{2}\left(-\alpha \pm \sqrt{\alpha^2 - 4}\right)t\right]. \tag{18}$$

If $\alpha \geq 2$, then the exponents are real, and both solutions decay exponentially, whereas if $\alpha < 2$, then the exponents are complex, and both solutions decay exponentially but at the rate set by the real part of the exponent. Figure 4 shows the decay of the transient solutions for the M_2 and K_1 filters in the first 25 days. It provides some guidance for determining the spin-up time that the filter equations need before their outputs can be considered as consisting of tidal signals only.

3.3. Discretization Errors

Numerically, the filter equations (Equation 11) can be implemented using, for example, the following time stepping algorithm,

$$s_1^{(n)} = \omega_1\Delta t u_1^{(n-1)} + s_1^{(n-1)}, \tag{19a}$$

$$u_1^{(n)} = -\omega_1\Delta t\left[s_1^{(n)} - \alpha u^{(n)}\right] + (1 - \alpha\omega_1\Delta t)\,u_1^{(n-1)}. \tag{19b}$$

Here, the superscripts (n) and $(n-1)$ represent the current and previous time steps, respectively, and Δt is the time step size. Note that the dummy variable s_1 is evaluated first, in order for u_1 to be evaluated based on the value of s_1 at the current time step. While only the continuous time has been considered in the analyses so far, discretization of the time domain will lead to errors of both amplitude and phase in the output signals, even at the target frequency of the filter.

19422466, 2024, 10, Downloaded from https://agupubs.onlinelibrary.wiley.com/doi/10.1029/2024MS004319, Wiley Online Library on [12/06/2025]. See the Terms and Conditions (https://onlinelibrary.wiley.com/terms-and-conditions) on Wiley Online Library for rules of use; OA articles are governed by the applicable Creative Commons License

19422466, 2024, 10, Downloaded from https://agupubs.onlinelibrary.wiley.com/doi/10.1029/2024MS004319, Wiley Online Library on [12/06/2025]. See the Terms and Conditions (https://onlinelibrary.wiley.com/terms-and-conditions) on Wiley Online Library for rules of use; OA articles are governed by the applicable Creative Commons License

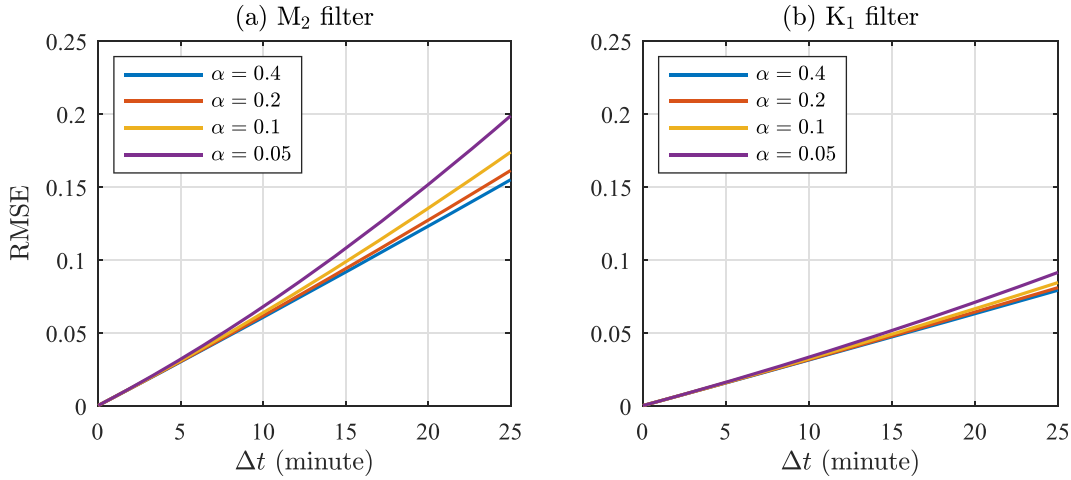

Figure 5. Discretization error as a function of the time step size, Δt, measured in terms of the root mean squared error of the numerical solutions computed against the exact solution with unit amplitude.

As an example, consider the input signal given by

$$u(t) = \cos(\omega_1 t), \tag{20}$$

whose frequency is the same as the target frequency of the filter. Without discretization error, the output of the filter should be identical to the input, that is, $u_1(t) = u(t)$ for all t. Hence, the discretization error can be quantified by calculating the RMSE of the numerical solutions against the exact solution. Figure 5 shows that the discretization error scales approximately linearly with Δt, which is expected for a first-order time stepping scheme. For a given Δt, the discretization error increases as α decreases, though this increase is insignificant for small Δt. The discretization error is also frequency dependent. Given the same Δt and α, the error tends to be larger for higher-frequency signals. In this particular example, the amplitude of the input signal is unity. Hence, the RMSE plotted in Figure 5 may be interpreted in terms of percentage. We have also performed additional tests and found that the discretization error is independent of phase change. Given a desired precision level, Figure 5 thus provides some guidance for determining Δt of the filter equations. Note that Δt does not have to be the same as the time step size adopted by the model, as long as the model output is available as input for the filter equations.

4. Numerical Simulations

4.1. Model Description

In this section, the filter equations (Equation 19) are incorporated into MOM6 to demonstrate its application to the parameterization of frequency-dependent internal wave drag. MOM6 is a three-dimensional primitive equation numerical model, developed at the Geophysical Fluid Dynamics Laboratory (GFDL) of the National Oceanic and Atmospheric Administration (NOAA) for long-term integration and climate studies (Adcroft et al., 2019). In this work, a barotropic version of the global model was configured, which solves the one-layer shallow water momentum and continuity equations,

$$\frac{D\mathbf{u}}{Dt} + f\mathbf{k}\times\mathbf{u} = -g\nabla\left(\eta - \eta_{\text{eq}} - \eta_{\text{SAL}}\right) - \frac{C_D|\mathbf{u}|\mathbf{u}}{H} - \frac{\mathbb{C}\cdot\mathbf{u}}{H}, \tag{21a}$$

$$\frac{D\eta}{Dt} = -\nabla\cdot[(H+\eta)\mathbf{u}]. \tag{21b}$$

In these equations, $\mathbf{u}$ is the horizontal velocity, η is the perturbation tidal elevation, η_{eq} is the equilibrium tidal potential, η_{SAL} is the self-attraction and loading term, g is the acceleration due to gravity, f is the Coriolis frequency, $\mathbf{k}$ is the vertical unit vector, H is the resting water depth, C_D is the bottom drag coefficient, and $\mathbb{C}$ is the

19422466, 2024, 10, Downloaded from https://agupubs.onlinelibrary.wiley.com/doi/10.1029/2024MS004319, Wiley Online Library on [12/06/2025]. See the Terms and Conditions (https://onlinelibrary.wiley.com/terms-and-conditions) on Wiley Online Library for rules of use; OA articles are governed by the applicable Creative Commons License

internal wave drag tensor. The model is configured on a tri-polar grid with a $1/12°$ nominal resolution, adapted from the "GLBc0.08" configuration of the Hybrid Coordinate Ocean Model (HYCOM; Bleck, 2002). The bottom and under-ice-shelf topography is adapted from the NOAA Global Storm Surge and Tide Operational Forecast model (G-STOFS; Blakely et al., 2022). The barotropic tides are forced by the astronomical tidal potential at the M_2 and K_1 frequencies and are modified by the term η_{SAL} to include the effects of ocean self-attraction and solid-earth loading (Egbert & Erofeeva, 2002). The baroclinic tides are parameterized based on the scheme developed by Jayne and St. Laurent (2001), who suggested that the internal wave drag tensor, $\mathbb{C}$, can be approximated by a simple linear drag coefficient

$$C_{\mathrm{JSL}} = \frac{\pi \hat{h}^2 N_b}{L}, \tag{22}$$

where L is the topographic length scale, $\hat{h}$ is the topographic roughness scale, and N_b is the buoyancy frequency along the ocean bottom.

In our simulations, the barotropic velocity was filtered at the M_2 and K_1 frequencies, so that internal wave drag can be applied to the M_2 and K_1 velocities. This involves modifications to the MOM6 barotropic solver by replacing the momentum equation with

$$\frac{D\mathbf{u}}{Dt} + f\mathbf{k}\times\mathbf{u} = -g\nabla\left(\eta - \eta_{\mathrm{eq}} - \eta_{\mathrm{SAL}}\right) - \frac{C_D|\mathbf{u}|\mathbf{u}}{H} - \frac{C_{\mathrm{JSL}}}{H}\left(\kappa_{M2}\mathbf{u}_{M2} + \kappa_{K1}\mathbf{u}_{K1}\right), \tag{23}$$

where $\mathbf{u}_{M2}$ and $\mathbf{u}_{K1}$ represent the M_2 and K_1 band-passed velocities obtained from the filtering, while κ_{M2} and κ_{K1} are the dimensionless scaling factors, controlling the internal wave drag applied to the semi-diurnal and diurnal frequency bands, respectively. For both M_2 and K_1 filters, α was set to 0.1, so that the proportion of diurnal (semi-diurnal) signal that can pass through the M_2 (K_1) filter is about 0.25% (see Table 1), while the spin-up times for the M_2 and K_1 filter equations are about 7.5 and 15 days, respectively. At the end of the spin-up time, the amplitude of the transient solution is expected to be less than 1% of its initial value.

4.2. Simulation Results

Based on the linear theory (Bell, 1975a, 1975b; Llewellyn Smith & Young, 2002), the scaling factors κ_{M2} and κ_{K1} are of the form $\sqrt{1-f^2/\omega^2}$ and are latitude dependent. In our simulations, for clarity of presentation and for the purpose of demonstrating the application of the filters, spatially uniform values of κ_{M2} and κ_{K1} were adopted. The numerical simulations were performed with either $\kappa_{M2} = 0$ or $\kappa_{K1} = 0$ and the other scaling factor varied between 0 and 2. The simulation results were compared against the TPXO9 data (Egbert & Erofeeva, 2002) by computing the RMSE of the tidal elevation,

$$\mathrm{RMSE} = \sqrt{0.5\left(C_m^2 + C_T^2\right) - C_m C_T \cos\left(\theta_m - \theta_T\right)}, \tag{24}$$

where the subscripts m and T refer to the model results and TPXO data, respectively. From model output, tidal amplitudes and phases were obtained by performing harmonic analysis on the sea surface height from day 16 to day 30. Then, the global mean RMSE of the M_2 and K_1 elevations were taken over all depths and latitudes, as well as waters deeper than 1,000 m. The global mean RMSE is defined by

$$\overline{\mathrm{RMSE}} = \sqrt{\frac{\sum \mathrm{RMSE}^2 \Delta A}{\sum \Delta A}}, \tag{25}$$

where ΔA represents the area of each grid cell.

Tables 2 and 3 show that the variation of the scaling factors has a systematic effect on the RMSE calculated at their target frequency band but very little

Table 2
Global Mean Root Mean Squared Error of M_2 *and* K_1 *Elevations (cm) for All Depths and Deep Waters, With* $\kappa_{K1} = 0$ *and* κ_{M2} *Varying Between 0 and 2*

κ_{M2}	0	0.25	0.5	0.75	1	1.25	1.5	1.75	2
M_2, all depths	11.39	8.54	6.64	5.73	5.77	6.47	7.48	8.58	9.67
M_2, deep waters	9.54	6.69	4.67	3.65	3.79	4.67	5.80	6.95	8.05
K_1, all depths	3.42	3.39	3.36	3.35	3.34	3.33	3.33	3.33	3.32
K_1, deep waters	2.39	2.37	2.35	2.34	2.33	2.33	2.32	2.32	2.32

Note. Visualization is provided in Figure 6a.

19422466, 2024, 10, Downloaded from https://agupubs.onlinelibrary.wiley.com/doi/10.1029/2024MS004319, Wiley Online Library on [12/06/2025]. See the Terms and Conditions (https://onlinelibrary.wiley.com/terms-and-conditions) on Wiley Online Library for rules of use; OA articles are governed by the applicable Creative Commons License

Table 3
Global Mean Root Mean Squared Error of M_2 *and* K_1 *Elevations (cm) for All Depths and Deep Waters, With* $\kappa_{M2} = 0$ *and* κ_{K1} *Varying Between 0.25 and 2*

κ_{K1}	0.25	0.5	0.75	1	1.25	1.5	1.75	2
M_2, all depths	11.42	11.45	11.48	11.52	11.56	11.60	11.64	11.68
M_2, deep waters	9.55	9.57	9.59	9.61	9.63	9.66	9.68	9.71
K_1, all depths	2.95	2.60	2.37	2.27	2.28	2.36	2.51	2.70
K_1, deep waters	1.95	1.62	1.42	1.36	1.41	1.56	1.75	1.96

Note. Visualization is provided in Figure 6b.

influence on the RMSE calculated from the off-target frequency band. This suggests that the filters were performing as expected during the simulations, allowing us to control the internal wave drag applied to the semi-diurnal and diurnal frequency bands separately. Moreover, Figure 6 shows that the RMSE appears as a convex function of the scaling factor imposed on the filter's target frequency band. For the RMSE of M_2 elevation, the local minimum occurs when κ_{M2} is between 0.75 and 1, and the minimum value is smaller than that in the simulation where the drag is applied to the unfiltered velocity field. For the RMSE of K_1 elevation, the local minimum occurs when κ_{K1} is between 1 and 1.25, and the minimum value is marginally larger than that in the simulation where the drag is applied to the unfiltered velocity field. The fact that the local minima of the RMSE of M_2 and K_1 elevations occur at different values of κ_{M2} and κ_{K1} suggests that the optimally tuned internal wave drag for the semi-diurnal and diurnal frequency bands should be different, which is consistent with theoretical analyses reported in the past literature (Bell, 1975a, 1975b; Llewellyn Smith & Young, 2002; Nycander, 2005).

5. Conclusions

In this work, we developed a computationally efficient algorithm for constructing streaming band-pass filters that are capable of detecting the instantaneous tidal signals and their temporal variations in numerical simulations performed in the time domain. The filter equations consist of a system of two coupled ordinary differential equations, which takes the instantaneous model output at the current time step as the input and then filters the input signal based on the pre-determined target frequency and bandwidth. Analyses in Fourier space show that the filter's response to a broadband input is unity at its target frequency and vanishes toward both low and high-frequency limits. The decay of the filter response away from the target frequency is symmetric about the

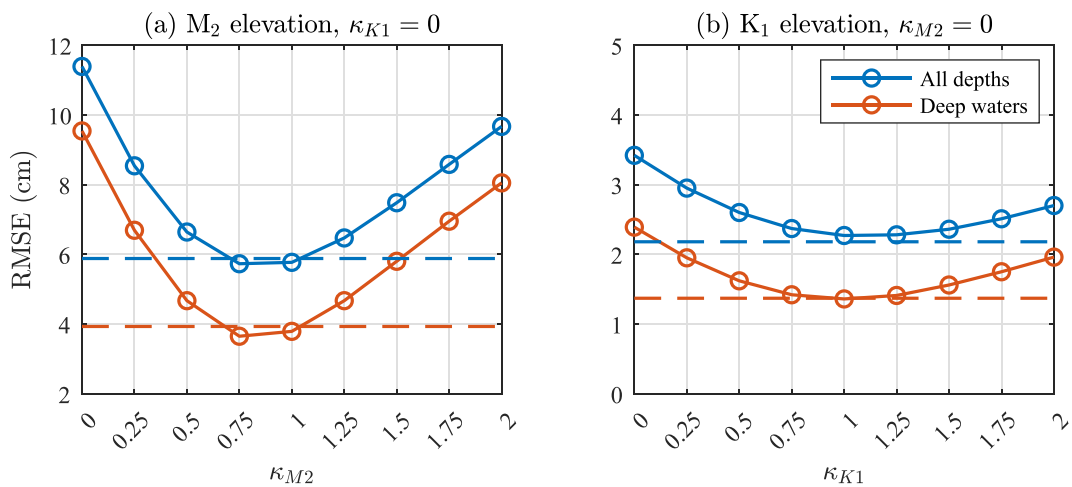

Figure 6. Global mean root mean squared error (RMSE) of (a) M_2 elevation and (b) K_1 elevation for all depths (blue) and deep waters only (red), reproduced from Tables 2 and 3. Solid curves indicate results from simulations in which frequency-dependent wave drag is applied to the filtered velocity fields. Dashed lines indicate results from the simulation in which the wave drag is applied to the unfiltered velocity field, where the global mean RMSE of M_2 elevation are 5.88 cm for all depths and 3.93 cm for deep waters, while the global mean RMSE of K_1 elevation are 2.18 cm for all depths and 1.37 cm for deep waters.

target frequency in the log-linear scale of the frequency spectrum, and the rate of decay is controlled by a dimensionless parameter that determines the filter's bandwidth.

The filter equations are incorporated into the barotropic solver of MOM6 and are used for determining the instantaneous tidal velocities at the M_2 and K_1 frequencies, in order to demonstrate the application of the band-pass filtering to the parameterization of frequency-dependent internal wave drag. The algorithm is validated by the simulation results, which suggest that the drag has a systematic effect on the dynamics at the filter's target frequency band but very little influence at the off-target frequency band.

There are several major differences between the conventional harmonic analysis and the band-pass filtering. Essentially, the former decomposes the input signal into trigonometric series and searches for least-square solutions that can be interpreted in terms of tidal amplitudes and phases, whereas the latter simply outputs time series consisting of sinusoidal motions, where information of amplitudes and phases is not directly available. Moreover, harmonic constants determined from the conventional harmonic analysis are time-independent, whereas the band-pass filtering is a streaming process, and the filter's output adjusts to the input signal dynamically during the time-stepping. This makes the band-pass filtering particularly suitable for capturing the seasonal variability of tides.

The filtering algorithm developed in this work is based on a system of equations that can be represented in terms of a second-order linear ordinary differential equation. For future works, high order systems of differential equations can be considered, which may allow for separate control of the filter's bandwidth and sharpness (Schaumann et al., 2009), so that more signal within the filter's target frequency band may pass through while more signal outside of the target frequency band is blocked.

Appendix A: Proofs of Theorems

A1. Proof of Theorem 1

If either $\alpha = 0$ or $\beta = 0$, then we can simply let $\beta = 0$ and $\alpha > 0$ without loss of generality. By letting $\Omega = \ln \omega$, the filter transfer function can be written as

$$\mathcal{A}(\Omega;\alpha) = \frac{i\alpha e^{\Omega}}{(1 - e^{2\Omega}) + i\alpha e^{\Omega}}, \tag{A1}$$

whose real and imaginary parts are given by

$$\Re(\mathcal{A}) = \frac{\alpha^2 e^{2\Omega}}{(1 - e^{2\Omega})^2 + \alpha^2 e^{2\Omega}}, \quad \text{and} \quad \Im(\mathcal{A}) = \frac{\alpha e^{\Omega}(1 - e^{2\Omega})}{(1 - e^{2\Omega})^2 + \alpha^2 e^{2\Omega}}, \tag{A2}$$

respectively. It follows that

$$\begin{aligned} \Re[\mathcal{A}(-\Omega;\alpha)] &= \frac{\alpha^2 e^{-2\Omega}}{(1 - e^{-2\Omega})^2 + \alpha^2 e^{-2\Omega}} \\ &= \frac{\alpha^2 e^{2\Omega}}{e^{4\Omega}\left[(1 - e^{-2\Omega})^2 + \alpha^2 e^{-2\Omega}\right]} \\ &= \frac{\alpha^2 e^{2\Omega}}{(e^{2\Omega} - 1)^2 + \alpha^2 e^{2\Omega}} \\ &= \Re[\mathcal{A}(\Omega;\alpha)], \end{aligned} \tag{A3}$$

and that

19422466, 2024, 10, Downloaded from https://agupubs.onlinelibrary.wiley.com/doi/10.1029/2024MS004319, Wiley Online Library on [12/06/2025]. See the Terms and Conditions (https://onlinelibrary.wiley.com/terms-and-conditions) on Wiley Online Library for rules of use; OA articles are governed by the applicable Creative Commons License

19422466, 2024, 10, Downloaded from https://agupubs.onlinelibrary.wiley.com/doi/10.1029/2024MS004319, Wiley Online Library on [12/06/2025]. See the Terms and Conditions (https://onlinelibrary.wiley.com/terms-and-conditions) on Wiley Online Library for rules of use; OA articles are governed by the applicable Creative Commons License

$$\begin{aligned}\Im[\mathcal{A}(-\Omega;\alpha)] &= \frac{\alpha e^{-\Omega}\left(1-e^{-2\Omega}\right)}{\left(1-e^{-2\Omega}\right)^2+\alpha^2 e^{-2\Omega}} \\ &= \frac{\alpha e^{3\Omega}\left(1-e^{-2\Omega}\right)}{e^{4\Omega}\left[\left(1-e^{-2\Omega}\right)^2+\alpha^2 e^{-2\Omega}\right]} \\ &= \frac{\alpha e^{\Omega}\left(e^{2\Omega}-1\right)}{\left(e^{2\Omega}-1\right)^2+\alpha^2 e^{2\Omega}} \\ &= -\Im[\mathcal{A}(\Omega;\alpha)].\end{aligned} \tag{A4}$$

This implies that $\Re(\mathcal{A})$ is reflectional symmetric about $\Omega = 0$, while $\Im(\mathcal{A})$ is rotational symmetric about $\Omega = 0$. From the definitions of $|\mathcal{A}|$ and $\arg(\mathcal{A})$, this also implies that

$$|\mathcal{A}(-\Omega;\alpha)| = |\mathcal{A}(\Omega;\alpha)|, \quad \text{and} \quad \arg[\mathcal{A}(-\Omega;\alpha)] = -\arg[\mathcal{A}(\Omega;\alpha)], \tag{A5}$$

which means that $|\mathcal{A}|$ is reflectional symmetric about $\Omega = 0$, while $\arg(\mathcal{A})$ is rotational symmetric about $\Omega = 0$.

If α and β are both non-zero, then the proof of Theorem 3 (Appendix A3) implies that $\Re(\mathcal{A})$, $\Im(\mathcal{A})$, and $|\mathcal{A}|$ are all asymmetric. To show that $\Im(\mathcal{A})$ is also asymmetric about $\Omega = 0$, we shall rewrite $\Im(\mathcal{A})$ in terms of

$$\Im[\mathcal{A}(\Omega;\alpha,\beta)] = \frac{(\alpha+\beta)e^{\Omega}\left(1-e^{2\Omega}\right)}{(\alpha\beta+1-e^{2\Omega})^2+(\alpha+\beta)^2 e^{2\Omega}}. \tag{A6}$$

It follows that

$$\begin{aligned}\Im[\mathcal{A}(-\Omega;\alpha,\beta)] &= \frac{(\alpha+\beta)e^{-\Omega}\left(1-e^{-2\Omega}\right)}{(\alpha\beta+1-e^{-2\Omega})^2+(\alpha+\beta)^2 e^{-2\Omega}} \\ &= \frac{(\alpha+\beta)e^{3\Omega}\left(1-e^{-2\Omega}\right)}{e^{4\Omega}\left[(\alpha\beta+1-e^{-2\Omega})^2+(\alpha+\beta)^2 e^{-2\Omega}\right]} \\ &= \frac{(\alpha+\beta)e^{\Omega}\left(e^{2\Omega}-1\right)}{(\alpha\beta e^{2\Omega}+e^{2\Omega}-1)^2+(\alpha+\beta)^2 e^{2\Omega}}.\end{aligned} \tag{A7}$$

However, this does not equal to either $\Im[\mathcal{A}(\Omega;\alpha,\beta)]$ or $-\Im[\mathcal{A}(\Omega;\alpha,\beta)]$. Therefore, $\Im(\mathcal{A})$ is neither reflectional symmetric nor rotational symmetric about $\Omega = 0$.

A2. Proof of Theorem 2

Let $\beta = 0$. An expression of $|\mathcal{A}|$ is given by

$$|\mathcal{A}(\omega;\alpha)| = \frac{\alpha\omega}{\sqrt{(1-\omega^2)^2+\alpha^2\omega^2}}. \tag{A8}$$

From this expression, we can determine the first derivative of $|\mathcal{A}|$ with respect to ω,

$$\frac{d}{d\omega}|\mathcal{A}(\omega;\alpha)| = \frac{\alpha\left(1-\omega^4\right)}{\left[(1-\omega^2)^2+\alpha^2\omega^2\right]^{3/2}}. \tag{A9}$$

Since $\omega \geq 0$, this implies that there exists only one local extremum, which is $|\mathcal{A}| = 1$ and occurs at $\omega = 1$. Moreover, Theorem 3 states that $|\mathcal{A}|$ vanishes in both low and high frequency limits. Therefore, $|\mathcal{A}| = 1$ must be the global maximum.

If α and β are both non-zero, then we can define a constant c through

$$c = \frac{\omega^2 - 1}{\alpha\beta} \quad \Longleftrightarrow \quad \omega^2 - 1 = \alpha\beta c. \tag{A10}$$

With some algebra, we can obtain an expression for $|\mathcal{A}|$ represented in terms of c,

$$|\mathcal{A}(c;\alpha,\beta)| = \left[1 - \frac{\alpha^2\beta^2 c(c-2)}{\alpha^2\beta^2(c-1)^2 + (\alpha+\beta)^2(\alpha\beta c+1))}\right]^{1/2}. \tag{A11}$$

This expression suggests that $|\mathcal{A}| > 1$ if $c(c-2) < 0$, which can occur if $0 < c < 2$, or equivalently, if $1 < \omega < \sqrt{2\alpha\beta + 1}$. As long as α and β are both non-zero, such an interval always exists to the right of $\omega = 1$, implying that the maximum value of $|\mathcal{A}|$ is always greater than unity.

A3. Proof of Theorem 3

In the high-frequency limit, $\omega \gg 1$ and $\omega \gg \alpha\beta$, such that

$$\Re(\mathcal{A}) \approx \frac{-\alpha\beta\omega^2 + (\alpha+\beta)^2\omega^2}{\omega^4 + (\alpha+\beta)^2\omega^2} \approx \frac{(\alpha+\beta)^2 - \alpha\beta}{\omega^2}, \quad \Rightarrow \quad \lim_{\omega\to\infty}\Re(\mathcal{A}) = 0^+, \tag{A12}$$

and

$$\Im(\mathcal{A}) \approx -\frac{\omega^3(\alpha+\beta)}{\omega^4 + (\alpha+\beta)^2\omega^2} \approx -\frac{\alpha+\beta}{\omega}, \quad \Rightarrow \quad \lim_{\omega\to\infty}\Im(\mathcal{A}) = 0^-. \tag{A13}$$

Since $\Re(\mathcal{A}) \sim \mathcal{O}(\omega^{-2})$ while $\Im(\mathcal{A}) \sim \mathcal{O}(\omega^{-1})$, from the definition of $|\mathcal{A}|$, this implies that $|\mathcal{A}| \sim \mathcal{O}(\omega^{-1})$, and that

$$\lim_{\omega\to\infty}|\mathcal{A}| = 0^+. \tag{A14}$$

Moreover, since $\frac{\Im(\mathcal{A})}{\Re(\mathcal{A})} \sim \mathcal{O}(\omega)$, while $\Re(\mathcal{A}) > 0$ and $\Im(\mathcal{A}) < 0$, this also implies that

$$\lim_{\omega\to\infty}\frac{\Im(\mathcal{A})}{\Re(\mathcal{A})} \to -\infty, \quad \Rightarrow \quad \lim_{\omega\to\infty}\arg(A) = -\frac{\pi}{2}. \tag{A15}$$

Note that the above limiting behaviors hold for all $\alpha \geq 0$ and $\beta \geq 0$.

In the low-frequency limit, we shall first assume that α and β are both non-zero, such that $\omega \ll 1$ and $\omega \ll \alpha\beta$. In this case,

$$\Re(\mathcal{A}) \approx \frac{\alpha\beta(\alpha\beta+1) + (\alpha+\beta)^2\omega^2}{(\alpha\beta+1)^2 + (\alpha+\beta)^2\omega^2} \approx \frac{\alpha\beta}{\alpha\beta+1}, \tag{A16}$$

and

$$\Im(\mathcal{A}) \approx \frac{\omega(\alpha+\beta)}{(\alpha\beta+1)^2 + (\alpha+\beta)^2\omega^2} \approx \frac{\omega(\alpha+\beta)}{(\alpha\beta+1)^2}, \quad \Rightarrow \quad \lim_{\omega\to 0}\Im(\mathcal{A}) = 0^+. \tag{A17}$$

This suggests that $\Re(\mathcal{A})$ does not vanish but approaches some constant determined by α and β. As a result, $|\mathcal{A}|$ does not vanish either. Moreover, this implies that

$$\frac{\Im(\mathcal{A})}{\Re(\mathcal{A})} \sim \mathcal{O}(\omega), \quad \Rightarrow \quad \lim_{\omega\to 0}\frac{\Im(\mathcal{A})}{\Re(\mathcal{A})} = 0^+, \quad \Rightarrow \quad \lim_{\omega\to 0}\arg(A) = 0^+. \tag{A18}$$

19422466, 2024, 10, Downloaded from https://agupubs.onlinelibrary.wiley.com/doi/10.1029/2024MS004319, Wiley Online Library on [12/06/2025]. See the Terms and Conditions (https://onlinelibrary.wiley.com/terms-and-conditions) on Wiley Online Library for rules of use; OA articles are governed by the applicable Creative Commons License

19422466, 2024, 10, Downloaded from https://agupubs.onlinelibrary.wiley.com/doi/10.1029/2024MS004319, Wiley Online Library on [12/06/2025]. See the Terms and Conditions (https://onlinelibrary.wiley.com/terms-and-conditions) on Wiley Online Library for rules of use; OA articles are governed by the applicable Creative Commons License

If either $\alpha = 0$ or $\beta = 0$, then we can let $\beta = 0$ as we did before. In this case,

$$\Re(\mathcal{A}) \approx \frac{\alpha^2\omega^2}{1+\alpha^2\omega^2} \approx \alpha^2\omega^2, \quad \Rightarrow \quad \Re(\mathcal{A}) \sim \mathcal{O}(\omega^2), \quad \text{and} \quad \lim_{\omega\to 0}\Re(\mathcal{A}) = 0^+, \tag{A19}$$

and

$$\Im(\mathcal{A}) \approx \frac{\alpha\omega}{1+\alpha^2\omega^2} \approx \alpha\omega, \quad \Rightarrow \quad \Im(\mathcal{A}) \sim \mathcal{O}(\omega), \quad \text{and} \quad \lim_{\omega\to 0}\Im(\mathcal{A}) = 0^+. \tag{A20}$$

This implies that

$$|\mathcal{A}| \sim \mathcal{O}(\omega), \quad \Rightarrow \quad \lim_{\omega\to 0}|\mathcal{A}| = 0^+, \tag{A21}$$

and that

$$\frac{\Im(\mathcal{A})}{\Re(\mathcal{A})} \sim O(\omega^{-1}), \quad \Rightarrow \quad \lim_{\omega\to 0}\frac{\Im(\mathcal{A})}{\Re(\mathcal{A})} = \infty, \quad \Rightarrow \quad \lim_{\omega\to 0}\arg(A) = \frac{\pi}{2}. \tag{A22}$$

Data Availability Statement

Implementation of the streaming filters and the frequency-dependent drag in MOM6 can be found at https://github.com/c2xu/MOM6/releases/tag/v1.0.0 (Xu, 2024).

Acknowledgments
This work was supported by the U. S. National Oceanic and Atmospheric Administration through Grant NA22OAR0110487 to Oregon State University. The authors thank Alan Wallcraft and He Wang for providing the GLBc0.08 configuration and Jay Shriver for generating the internal wave drag coefficients. The authors also thank the associate editor and the three anonymous referees for their constructive comments and suggestions that led to significant improvement of this work.

References

Adcroft, A., Anderson, W., Balaji, V., Blanton, C., Bushuk, M., Dufour, C. O., et al. (2019). The GFDL global ocean and sea ice model OM4.0: Model description and simulation features. *Journal of Advances in Modeling Earth Systems*, *11*(10), 3167–3211. https://doi.org/10.1029/2019MS001726

Arbic, B. K. (2022). Incorporating tides and internal gravity waves within global ocean general circulation models: A review. *Progress in Oceanography*, *206*, 102824. https://doi.org/10.1016/j.pocean.2022.102824

Bell, T. H. (1975a). Lee waves in stratified flows with simple harmonic time dependence. *Journal of Fluid Mechanics*, *67*(4), 705–722. https://doi.org/10.1017/S0022112075000560

Bell, T. H. (1975b). Topographically generated internal waves in the open ocean. *Journal of Geophysical Research*, *80*(3), 320–327. https://doi.org/10.1029/JC080i003p00320

Blakely, C. P., Ling, G., Pringle, W. J., Contreras, M. T., Wirasaet, D., Westerink, J. J., et al. (2022). Dissipation and bathymetric sensitivities in an unstructured mesh global tidal model. *Journal of Geophysical Research: Oceans*, *127*(5), e2021JC018178. https://doi.org/10.1029/2021JC018178

Bleck, R. (2002). An oceanic general circulation model framed in hybrid isopycnic-Cartesian coordinates. *Ocean Modelling*, *4*(1), 55–88. https://doi.org/10.1016/S1463-5003(01)00012-9

Buijsman, M. C., Ansong, J. K., Arbic, B. K., Richman, J. G., Shriver, J. F., Timko, P. G., et al. (2016). Impact of parameterized internal wave drag on the semidiurnal energy balance in a global ocean circulation model. *Journal of Physical Oceanography*, *46*(5), 1399–1419. https://doi.org/10.1175/JPO-D-15-0074.1

Egbert, G. D., & Erofeeva, S. Y. (2002). Efficient inverse modeling of barotropic ocean tides. *Journal of Atmospheric and Oceanic Technology*, *19*(2), 183–204. https://doi.org/10.1175/1520-0426(2002)019⟨0183:EIMOBO⟩2.0.CO;2

Egbert, G. D., & Ray, R. D. (2000). Significant dissipation of tidal energy in the deep ocean inferred from satellite altimeter data. *Nature*, *405*(6788), 775–778. https://doi.org/10.1038/35015531

Egbert, G. D., & Ray, R. D. (2001). Estimates of M2 tidal energy dissipation from TOPEX/Poseidon altimetry data. *Journal of Geophysical Research*, *106*(C10), 22475–22502. https://doi.org/10.1029/2000JC000699

Egbert, G. D., & Ray, R. D. (2003). Semi-diurnal and diurnal tidal dissipation from TOPEX/Poseidon altimetry. *Geophysical Research Letters*, *30*(17), 1907. https://doi.org/10.1029/2003GL017676

Foreman, M. G. G., Cherniawsky, J. Y., & Ballantyne, V. A. (2009). Versatile harmonic tidal analysis: Improvements and applications. *Journal of Atmospheric and Oceanic Technology*, *26*(4), 806–817. https://doi.org/10.1175/2008JTECHO615.1

Garner, S. T. (2005). A topographic drag closure built on an analytical base flux. *Journal of the Atmospheric Sciences*, *62*(7), 2302–2315. https://doi.org/10.1175/JAS3496.1

Jayne, S. R., & St. Laurent, L. C. (2001). Parameterizing tidal dissipation over rough topography. *Geophysical Research Letters*, *28*(5), 811–814. https://doi.org/10.1029/2000GL012044

Llewellyn Smith, S. G., & Young, W. R. (2002). Conversion of the barotropic tide. *Journal of Physical Oceanography*, *32*(5), 1554–1566. https://doi.org/10.1175/1520-0485(2002)032⟨1554:COTBT⟩2.0.CO;2

Nycander, J. (2005). Generation of internal waves in the deep ocean by tides. *Journal of Geophysical Research*, *110*(C10), C10028. https://doi.org/10.1029/2004JC002487

Paquin, J.-P., Lu, Y., Taylor, S., Blanken, H., Marcotte, G., Hu, X., et al. (2020). High-resolution modelling of a coastal harbour in the presence of strong tides and significant river runoff. *Ocean Dynamics*, *70*(3), 365–385. https://doi.org/10.1007/s10236-019-01334-7

Rotermund, L. M., Williams, W. J., Klymak, J. M., Wu, Y., Scharien, R. K., & Haas, C. (2021). The effect of sea ice on tidal propagation in the Kitikmeot Sea, Canadian Arctic Archipelago. *Journal of Geophysical Research: Oceans*, *126*(5), e2020JC016786. https://doi.org/10.1029/2020JC016786

Schaumann, R., Xiao, H., & Van Valkenburg, M. (2009). *Design of analog filters*. *The Oxford Series in Electrical and Computer Engineering* (2nd ed.). Oxford University Press.

Trefethen, L. N., Birkisson, A., & Driscoll, T. A. (2018). *Exploring ODEs*. Society for Industrial and Applied Mathematics.

Xu, C. (2024). MOM6: Frequency-dependent drag (v1.0.0) [Dataset]. *Zenodo*. https://doi.org/10.5281/zenodo.13379023

Zaron, E. D., & Egbert, G. D. (2006). Estimating open-ocean barotropic tidal dissipation: The Hawaiian Ridge. *Journal of Physical Oceanography*, *36*(6), 1019–1035. https://doi.org/10.1175/JPO2878.1

19422466, 2024, 10, Downloaded from https://agupubs.onlinelibrary.wiley.com/doi/10.1029/2024MS004319, Wiley Online Library on [12/06/2025]. See the Terms and Conditions (https://onlinelibrary.wiley.com/terms-and-conditions) on Wiley Online Library for rules of use; OA articles are governed by the applicable Creative Commons License